

Effective Interaction Between Membrane And Scaffold

Masterarbeit aus der Physik

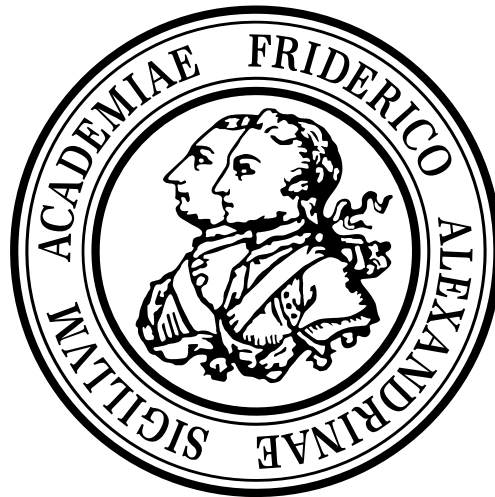
Vorgelegt von

Matthias Späth

04.02.2016

PULS Group

Friedrich-Alexander-Universität Erlangen-Nürnberg



Betreuung: Prof. Dr. Ana-Sunčana Smith

Summary

Life threatening and life forming events, like the spreading of cancer and embryogenesis, are governed by how cells interact with each other and therefore by cell adhesion. Further, all cells are surrounded by membranes. Therefore, the understanding of membrane interactions is the foundation for evaluating the role of biological membranes in the process of cell adhesion. While the role of various adhesive proteins in this process is mostly dealt with by biology, physics can be used to analyze and describe the mechanistic details of the membrane. This makes membranes and their interactions a highly relevant and exciting field in biophysics.

From a physical point of view the interaction between two opposing membranes or membrane and substrate is governed by the interaction potentials and the bending energy of the membrane. Even though the individual contributions, such as the Helfrich and steric repulsion, the van der Waals attraction, and the hydration forces are reasonably well understood, there is a discrepancy between the experimentally determined effective potential and its theoretical prediction. We address this discrepancy from several angles. We perform an in-depth analysis of the van der Waals interaction for membranes to make sure that there are no unexpected contributions for that potential. Additionally we construct real space Monte Carlo simulations for fluctuating membranes and their interactions. These are the two main chapters of this thesis.

While the van der Waals interaction for single molecules or atoms is of short range, it is one of the long-range interactions when it comes to opposing membranes. The strength of the interaction is governed by the Hamaker constant which is derived via Lifshitz calculation. The Lifshitz calculation is based on a summation of all energy modes to the total free energy and therefore takes the spatial assembly and dielectric properties of the interacting materials into account. We use Lifshitz calculations to derive the exact Hamaker constant for two different membrane-scaffold systems. The result shows a height dependence of the Hamaker constant, which is used for further simulations, and overall roughly reproduces the expected values for biological systems. Nevertheless, the findings don't explain the gap between experimental measurements and theoretical basis.

We implement Monte Carlo simulations to further address this discrepancy. The simulations include the membrane fluctuations governed by the bending energy and are described by the Helfrich Hamiltonian. Using these simulations, we reproduce previous results for membrane interactions with an impermeable wall and an external harmonic potential with excellent agreement. On top of that we show the influence of relevant parameters such as the bending rigidity, the Hamaker constant, the temperature, and the influence of steric repulsion. We close this chapter with a simulation that resembles recent experiments with as many details as possible, including the membrane fluctuations, steric repulsion, and the previously determined van der Waals potential. Thereby, we achieve unprecedented results in close proximity to the experimental findings for the average membrane height. We also reproduce a strong sensitivity for the parameter setting that was found in previous experiments.

All in all, the simulations give new insights on how the overall effective potential is determined and set limits to the common approximation of the effective potential, namely, the superposition of the individual attractive and repulsive contributions.

Contents

1	Introduction	4
1.1	Cells and Membranes	4
1.2	Interactions Between Membranes	7
2	Determination of the Hamaker Constant	11
2.1	Theoretical Background: Lifshitz Theory	11
2.2	Implementation of the Lifshitz Theory	14
2.2.1	Materials	15
2.2.2	Complete Setup	19
2.3	Results and Discussion	20
3	Effective Membrane Substrate Potential	26
3.1	Method: Monte Carlo Simulations	26
3.1.1	Validation with Harmonic Potential	28
3.1.2	Validation with Helfrich Repulsion	29
3.1.3	Finding a Proper External Potential	30
3.2	Results	33
3.3	Can we Reproduce Experiments?	37
4	Conclusions: Helfrich Repulsion and Additivity	40
5	Outlook	43

1 Introduction

Cell adhesion governs life threatening and life forming events by providing the basis for embryo morphogenesis and the spread of cancer at the same time, yet it is still not fully understood. On the one hand, cell adhesion describes the assembly of tissues, which is the basis for the formation of an embryo [1]. On the other hand, the spreading of cancer and metastasis is described by the cell-cell interaction of cancer cells with other cells. Therefore metastasis is partly governed by cell adhesion [2], and various adhesion molecules involved in the spreading have already been identified [3]. On top of these natural phenomena, cell adhesion plays an important role in drug delivery: drugs can be covered in molecules, which have the adhesive properties such that they can be deployed exactly where they are intended to be deployed, just like "Stealth bombers" [4]. The deployment can be, for instance, in a tumor cell or in an organ where the drug is supposed to operate. All in all, a detailed description of adhesion is essential for biological and medical understanding of various effects. To tackle the effects of adhesion we have to understand what a cell is and what role its components play.

1.1 Cells and Membranes

All living beings consist of cells which manage many processes, such as replication, signaling and adhesion [6]. For animals and humans we can specify even further, that they consist of eukaryotic cells which always have the same basic components, namely the nucleus, organelles, intracellular liquid and a surrounding plasma membrane [7] as shown in Figure 1. The main purpose of the surrounding membrane is to separate the inside of the cell from its environment. Membranes for eukaryotic cells consist of lipid molecules which are amphiphilic, that means they have a hydrophilic and a hydrophobic end [8]. Amphiphilic molecules automatically form bilayers or spherical micelles in water to minimize the hydrophobic tail-water interface [9]. In this thesis, we are focusing on lipid bilayers formed by phospholipids, which provide a good model

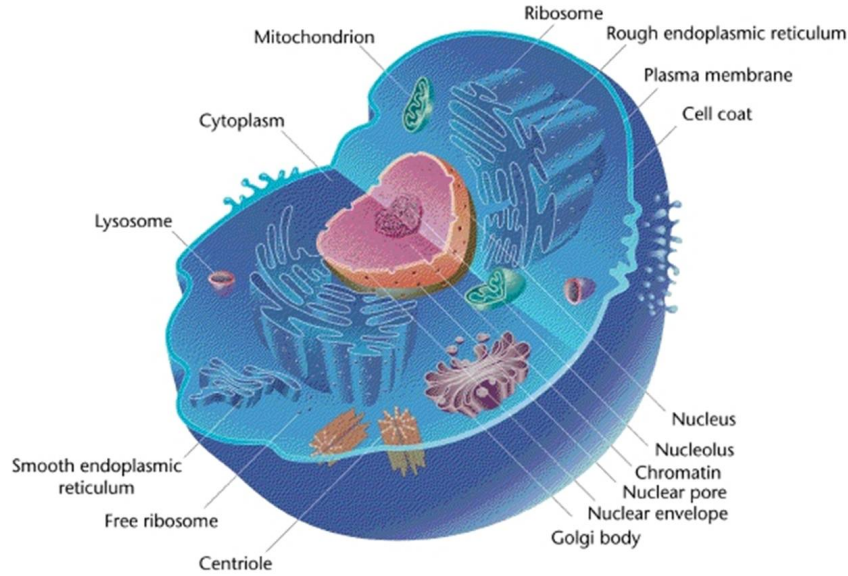


Figure 1: Eukaryotic cell with its main components: nucleus, various organelles, intracellular liquid and plasma membrane. Adopted from [5].

for cell-surface interaction [10]. The simplest way to analyze lipid bilayers is through idealized or model systems, such as giant unilamellar vesicles (GUVs) [11]. GUVs are essentially self-contained lipid bilayers that are filled with water or sucrose solution. The use of GUVs enables us to analyze the lipid bilayer while avoiding boundary effects caused by the cell interior. An example for a lipid bilayer is shown in Figure 2. Both bilayers have the hydrophobic tail on the inside and the hydrophilic headgroup on the outside of the bilayer.

As we try to model the membrane in a physical system, we need to find a way to describe the membrane without involving the description of every single lipid [12]. The lipid bilayer can be treated as a flat two dimensional surface. The focus of our analysis is the interaction of the membrane with a surface, and therefore we parametrize every point of the flat membrane by the height above the regarded surface. This leads to a parametrization $h(x)$, where $h(x)$ is the height above the surface and x is the projected position of the membrane on the surface. The description $h(x)$ is only distinct,

and therefore valid, when every position x on the surface has only one corresponding membrane height $h(x)$. This is the condition for the so-called Monge-representation of the membrane. The definiteness of $h(x)$ can also be guaranteed by the demand that the membrane is nearly planar or with the requirement that $\nabla h(x)$, the membrane's derivative, is small. The energetics of the membrane are described by a bending and a tension term. Membrane tension is linked to energy differences induced by a change of the membrane area. This phenomenon is not addressed in this thesis. Furthermore, we exclude fluctuation effects by active force centers, such as chemically active membrane proteins, in this approach [13, 14]. Hence, we only focus on the issue of bending, and neglect membrane tension and special effects through membrane proteins.

A vivid description for the bending energy is possible when looking at the membrane on the lipid level. When the membrane is bent downward, the upper lipid layer has to stretch and the lower lipid layer gets clinched. The energy cost that is covered by stretching and clinching the upper and lower part of the bilayer is the bending energy. A detailed derivation of the exact formula for the bending energy is based on differential geometry [15], and has the form shown by Helfrich in 1973 [16] of

$$E_B = \frac{\kappa}{2} \int_A dx (2H - c_0)^2, \quad (1)$$

where κ is the bending rigidity, H is the average bending energy of the membrane, and c_0 is the spontaneous curvature of the membrane. Spontaneous curvature is only relevant for membranes with sides that are chemically different and is equal to zero for a membrane with two similar lipid layers [17]. With the condition for the Monge representation that $\nabla h(r)$ is small from the last paragraph, we describe the average bending H by

$$H \approx \frac{1}{2} \nabla^2 h(r) \quad (2)$$

while sparing terms of a higher order than $(\nabla^2 h)$. Combining Equations 1 and 2 have

$$E_B \approx \frac{\kappa}{2} \int_A dx (\nabla^2 h(x))^2 \quad (3)$$

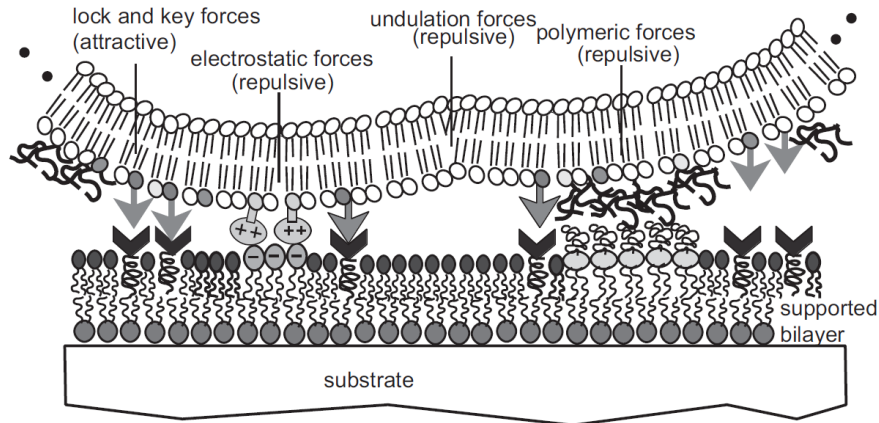


Figure 2: A fluctuating bilayer above a supported bilayer on substrate. Adopted from [7].

for the bending energy to second order. Equation 3 allows us to describe a fluctuating membrane only by its bending term.

Having addressed what a membrane is and how a freely fluctuating membrane can be described theoretically, the next step is to understand how a membrane interacts with its environment. Figure 2 illustrates how an experimental setup can look like. The bottom layer is the substrate, for instance glass, covered by a supported bilayer or BSA (bovine serum albumin), which is then interacting with the top layer, a floating membrane, through the water. The interaction is then described by the resulting height $h(x)$ and fluctuations of the membrane, which can be measured by IRM or RICM measurements. More information on the experimental background for IRM and RICM, including details on the height measurement, can be found in [18–25].

1.2 Interactions Between Membranes

To analyze the behavior of a membrane in an experiment, we have to take into account that a membrane is not floating freely, but is instead interacting with its environment. Various forms of these interactions are discussed in this chapter. Figure 2 shows the forces between membrane and scaffold: lock and key forces, electrostatic forces, undulation forces, polymeric forces, van der Waals forces, and gravity. All these forces balance at

the mean membrane height and, in other words, the total force is zero or the related potential has a minimum. To start an approach on how the total potential looks, we have to address the individual potentials first.

While the closing and opening of bonds in membrane-surface-interactions gives rise to interesting phenomena [26–29], we want to focus on the interactions which exist without bonds between membranes and surfaces. The membrane and substrate in our setup are coated such that they don't have any lock and key forces in the considered interaction area. This allows the membrane to fluctuate in the external potential without attachment to the substrate. Regardless some parts of the GUV are indeed attached to a scaffold, but our focus remains on the areas which are not attached.

Some parts of the membrane also give rise to electrostatic forces. Membranes can have charges on their head- or tail-groups rising from either charge groups dissociating from the membrane into the solution or ions from the solution binding to the membrane [30]. Due to the effect of screening through the water, the electrostatic interaction decays exponentially on the order of the Debye-Hückel screening length (approximately a few nanometers for our setup). A further contribution to this effect is hydration, which decays in the sub-nanometer range [31]. Both effects, electrostatic interaction and hydration, are neglected in this approach due to their short range.

Van der Waals forces are all forces between two permanent dipoles, permanent dipole and induced dipole, or two instantly induced dipoles. While these interactions between small molecules or atoms decay very steeply with distance (h^{-6}), the effect has a higher range for parallel surfaces [32]. This effect was shown by Hamaker and results in a decay rate of h^{-2} for two opposing half spaces [33]. The prefactor of the interaction was then named the Hamaker constant and the potential is described by

$$V_{vdW}(h) = -\frac{A_{Ham}}{12\pi} \frac{1}{h^2},$$

with A_{Ham} being the Hamaker constant and h being the distance between the surfaces. The non-additivity of the van der Waals interaction of all participating molecules and

atoms is avoided in the Lifshitz theory, where the free energy is calculated by an integral over all surface modes for the materials in case. The effect of the h^{-2} -decay makes the van der Waals force one of the long range interactions between membranes and is therefore particularly interesting for the analysis.

Helfrich repulsion is based on fluid membranes performing out-of-plane fluctuations that are described by their elastic resistance to curvature (cf. Equation 3) [34–38]. The fluctuations are hindered or suppressed when the membrane is close to a hard surface. This effect generates an entropic repulsion which is caused by the membrane hitting against the surface of the wall and therefore by restricting the volume for free fluctuations. This effect was found and described by Helfrich in 1978 [39] and gives rise to the repulsive Helfrich potential

$$V_H(h) = c_1 \frac{(k_B T)^2}{\kappa} \frac{1}{h^2}.$$

Hereby, κ is the bending rigidity of the membrane, h is the distance between membrane and surface, which suppresses the membrane's fluctuations, and c_1 is a numerical prefactor. At first, the prefactor c_1 was derived by rough theoretical approximations [39,40], but Bachmann et al. managed to calculate c_1 via variational perturbation theory up to third order, in great agreement with Monte Carlo simulations [41,42]. This provides a great basis to test implementations of membranes which should incorporate correct Helfrich repulsion. We will see that the Helfrich repulsion is one of the main contributors for the membrane-substrate interaction.

Polymeric forces are based on polymers that are attached to the membrane and play an important role as soon as they come in close contact with the environment of the membrane [43]. An example for a polymer attached to a membrane is PEG (polyethyleneglycol). The repulsive effect that comes from the polymers on the membrane was approximated by Bruinsma et al. [18] through

$$V_{PEG}(h) = \frac{\pi^2}{6} k_B T \rho_{PEG} \left(\frac{r_{PEG}}{h} \right)^2 e^{-\frac{3}{2} \left(\frac{h}{r_{PEG}} \right)^2}. \quad (4)$$

Thereby, ρ_{PEG} is the surface concentration and r_{PEG} is the radius of gyration of the PEG molecules. Polymeric repulsion provides one of the important repulsive forces right next to the Helfrich repulsion.

Gravitational forces also exist because the membrane is floating in water in the form of a vesicle which is filled with a solution. The density of the vesicle solution can differ from the density of the surrounding solution, which leads to gravitational effects. Another effect that comes into play is that the large vesicle can have some contact areas with the substrate (for instance by a supporting scaffold) that lower gravitational effects. In total this results in

$$V_{grav} = \frac{V}{A} \cdot \Delta\rho \cdot g \cdot h,$$

where V is the vesicle Volume, A the contact area of vesicle and grid and $\Delta\rho$ is the density difference between vesicle interior and exterior [25]. Even though gravity is not limited through the range of the interaction, it is weak compared to, for instance, the van der Waals interaction and is therefore neglected.

Having discussed all relevant interactions between membrane and substrate, we end up with three potentials that will play the most important role in this analysis: van der Waals, Helfrich and polymer repulsion potentials. Our first aim is to describe the van der Waals interaction for our specific system in great detail to exclude any surprises, such as repulsive behavior or a Hamaker constant that is inconsistent with expected values. The next step is then to describe a fluctuating membrane, which we implemented via Monte Carlo simulations. The final goal is the implementation of a fluctuating membrane in a system that includes all relevant external forces and thereby reproduces experimental results that were achieved in this field.

2 Determination of the Hamaker Constant

We have seen that one of the important interactions between membrane and scaffold is the van der Waals interaction. Being the most important attractive force in the system, the van der Waals interaction highly influences how the membrane behaves and is therefore addressed in great detail. The free energy for the van der Waals interaction between two half spaces is given by

$$G(h) = -\frac{A_{Ham}}{12\pi h^2},$$

with A_{Ham} being the Hamaker constant and h being the distance between the half spaces. It is important to note that A_{Ham} can, and in most cases will, be height dependent $A_{Ham}(h)$. Therefore the Hamaker constant $A_{Ham}(h)$ is the basis to describe the interaction for a given system [44, 45]. The determination of the Hamaker constant is only linked to the material properties and dimensions of the setup and is addressed using Lifshitz theory.

2.1 Theoretical Background: Lifshitz Theory

Lifshitz theory is the foundation for calculating the Hamaker constant and relies on the concept of summing up all energy modes to the total free energy. All electromagnetic-field fluctuations are decomposed into oscillatory modes which extend through the analyzed body and are restricted by the material properties and dimensions [46]. Merging the decomposition gives the total free energy. The total free energy is then linked to the van der Waals energy and hence the Hamaker constant can be estimated. A heuristic approach for the derivation of the Lifshitz theory, following Parsegian and Dagastine [44, 47], is given in this chapter. A descriptive illustration is a system of two materials facing each other through a medium and is presented in Figure 3. The free energy $G(h)$ is the sum of all free energies

$$G(h) = \sum_j g(\omega_j) \tag{5}$$

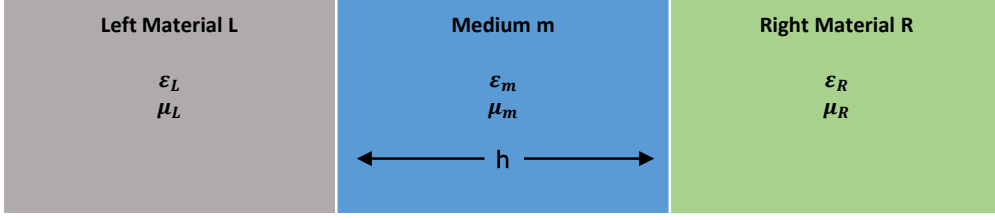


Figure 3: Example for the basis of Lifshitz calculations. Two materials (left L and right R) with their dielectric properties ϵ, μ are separated by medium m over a distance h. The interface of the materials is assumed to be infinite to avoid boundary effects on the edge. Further results are then given per unit area.

for the oscillations ω_j which are linked to the given boundary conditions for the system.

Following Equation 5 the first step in calculating the free energy is the determination of the allowed oscillations ω_j . The electric- and magnetic-fields are described in their Fourier components $E(t) = \text{Re}(\sum_{\omega} E_{\omega} e^{-i\omega t})$ and $H(t) = \text{Re}(\sum_{\omega} H_{\omega} e^{-i\omega t})$ respectively. The Fourier description enables us to apply the Maxwell equations as boundary conditions on E_{ω} and H_{ω} and hence link the surface modes to the given body and its material. For further steps, z is the direction perpendicular to the material interfaces. Due to periodicity in the x,y plane, each component of the E and H vectors have the general form $f(z)e^{i(ux+vy)}$. Therefore, the wave equation gives

$$\rho_i^2 = \rho^2 - \frac{\epsilon_i \mu_i \omega^2}{c^2} \quad (6)$$

for the radial wave vector ρ_i in each material, $i = L, m, R$ and $\rho^2 \equiv u^2 + v^2$ in the x,y plane. Gauss's law $\nabla E = \nabla H = 0$ gives the next boundary condition for the system:

$$1 - \left(\frac{\rho_L \epsilon_m - \rho_m \epsilon_L}{\rho_L \epsilon_m + \rho_m \epsilon_L} \right) \left(\frac{\rho_R \epsilon_m - \rho_m \epsilon_R}{\rho_R \epsilon_m + \rho_m \epsilon_R} \right) e^{-2\rho_m h} = 0. \quad (7)$$

Equations 6 and 7 describe the electrical surface modes fitting for the material, and the additional condition that

$$\rho^2 > \text{Re} \left(\frac{\epsilon_i \mu_i \omega^2}{c^2} \right) \quad (8)$$

ensures that excitations vanish for $z \rightarrow \infty$. Equations 6, 7, and 8 combined give conditions for all wave vectors and frequencies in our system and hence the first step of calculating all allowed oscillations is covered.

Now we calculate the free energy linked to each of the oscillations ω_j . For a nonclassical harmonic oscillator we have the energy levels

$$E_n = \hbar\omega_j \left(n + \frac{1}{2} \right), \quad (9)$$

with $n = 0, 1, 2, \dots$. The partition function for this oscillator is then described by

$$Z(\omega_j) = \sum_{n=0}^{\infty} e^{-E_n/k_B T}.$$

The free energy $g(\omega_j)$ for the oscillator in Equation 9 then goes as the logarithm of the partition function $Z(\omega_j)$

$$g(\omega_j) = -k_B T \log(Z(\omega_j)).$$

Putting the frequencies and their free energies together we have the free energy $G_h(h) = \sum_j g(\omega_j)$ and can calculate the total free energy by integrating over all wave vectors

$$G_{LmR}(h) = \frac{1}{(2\pi)^2} \text{Re} \left\{ \int_0^{\infty} 2\pi\rho [G_h(\rho) - G_{\infty}(\rho)] d\rho \right\}.$$

After further conversions for the evaluation of the integral we end up with the resulting formula for the total free energy of a system with material L , R separated by a medium m

$$G_{LmR}(h) = \frac{k_B T}{8\pi\hbar^2} \sum_{n=0}^{\infty \prime} \int_{r_n}^{\infty} x \ln[(1 - \bar{\Delta}_{Lm}\bar{\Delta}_{Rm}e^{-x})(1 - \Delta_{Lm}\Delta_{Rm}e^{-x})] dx, \quad (10)$$

with $\bar{\Delta}_{ji} = \frac{x_i\epsilon_j - x_j\epsilon_i}{x_i\epsilon_j + x_j\epsilon_i}$, $\Delta_{ji} = \frac{x_i\mu_j - x_j\mu_i}{x_i\mu_j + x_j\mu_i}$, $x_i^2 = x_m^2 + \left(\frac{2h\xi_n}{c}\right)^2 (\epsilon_i\mu_i - \epsilon_m\mu_m)$, the variable of integration $x = 2\rho_m h$, and $r_n = (2h\epsilon_m^{1/2}\mu_m^{1/2}/c)\xi_n$. ξ_n is related to the frequencies via $\omega = i\xi_n$. The \prime after the sum indicates that the zeroth term is summed up with the prefactor $\frac{1}{2}$, which comes from the method of integration. Detailed observation of

Equation 10 shows that it only requires the material dimensions and properties (in terms of ϵ and μ) for the evaluation.

The Hamaker constant A_{Ham} is defined as the prefactor that sums up the material dimensions and properties

$$G_{LmR}(h) = -\frac{A_{Ham}(h)}{12\pi h^2}. \quad (11)$$

By comparison of Equation 10 and 11, the Hamaker constant is given by the integral and the sum in Equation 10 multiplied by $-\frac{8k_B T}{12}$.

To apply Equation 10 for more complicated systems with multiple layers of materials separated by a medium, the formalism has to be applied recursively to each medium-medium edge, incorporating all boundary conditions [48]. The implementation of Equation 10 for multiple layers follows in the next chapter.

2.2 Implementation of the Lifshitz Theory

The implementation was provided by Drew Parsons to a great extent and follows the theoretical basis given in the previous chapter. However a short outline of the implementation, written in GNU Octave (version 3.8.2), is provided here. The implementation loops over the sum in Equation 10, thereby each summand provides the total free energy for one frequency. For each summand the integral over all wave vectors has to be evaluated, which means that for each wave vector all the material properties have to be calculated. The interlacing of a loop over an integral requires high computing power and in order to keep processing cost as low as possible we implemented the Gaussian Laguerre integration for the integral in Equation 10.

Gaussian Laguerre integration is a method that can be used when the function to be evaluated has a peak at $x = 1$, goes to zero as x goes to zero and tails off exponentially at large x . This is the case for the integrand given here [44]. The integral is then replaced by a sum weighted with Laguerre weights (cf. Equation 25.4.45 in [49]):

$$\int_0^\infty \exp(-x)f(x)dx = \sum_{i=1}^n \omega_i f(x_i) + R_n$$

Table 1: Evaluation of the Gaussian Laguerre integration (measured in time savings compared to performing the integral). 10 and 20 G.L. summands means that the first 10, respectively 20, summands with Laguerre weights were included in the sum.

	Integration	10 G.L. summands	20 G.L. summands
calculation time	100 %	8.4%	15.4%
error	0%	2.54×10^{-3}	5.65×10^{-5}

with the Gaussian Laguerre weight $\omega_i = \frac{x_i}{(n+1)^2(L_{n+1}(x_i))^2}$, the Laguerre polynomials $L_n(x)$, and x_i is the i^{th} zero of $L_n(x)$. The Laguerre weights ω_i are calculated once, tabulated, and used throughout all further calculations. Table 1 shows savings in calculation time with an example system of a membrane in water on titanium-coated silica. By using the Gaussian Laguerre integration, calculation time can be shortened by approximately one order of magnitude, while the deviation from the original results is negligible. This confirms that the Gaussian-Laguerre integration method converges quickly within the first few summands. Depending on the requirements for speed and accuracy, between 10 and 20 summands give reasonable results. For all further calculations the method with 20 Gaussian-Laguerre summands was used.

To solve the integral as described in the last paragraph, all the material properties have to be evaluated. The material properties are incorporated by the calculation of $\bar{\Delta}_{ji}$ and Δ_{ji} in Equation 10. This is done recursively for all layers of material in the system. The electromagnetic properties for all materials are collected from various tables and papers as described in more detail in the following chapter.

2.2.1 Materials

The dielectric function is required for all materials of the system: glass, water, BSA, PEG in water, and the membrane. As shown by Attard et al. [50], it is necessary to

take the details of the membrane into account and so the membrane is divided into a separate head- and tailgroup.

Glass

Starting from the bottom of the setup we start with the glass coverslip. Due to its size, the glass can be estimated as of infinite thickness. The dielectric function of the glass is implemented after Masuda et al. [51] for SiO_2

$$\epsilon_{Glass}(\omega) = 1 + \frac{C_{ir}}{1 + (\omega/\omega_{ir})^2} + \frac{C_{uv}}{1 + (\omega/\omega_{uv})^2}, \quad (12)$$

with ultraviolet absorption frequency $\omega_{uv} = 1.84 \times 10^{16}$ rad/s, infrared absorption frequency $\omega_{ir} = 1.74 \times 10^{14}$ rad/s, ultraviolet oscillator strength function $C_{uv} = 1.2601$, infrared oscillator strength function $C_{ir} = 1.5499$, and frequency ω . This result was obtained experimentally by means of an optical method and the dielectric function was then determined by use of the Kramer-Kronig relations [51].

Water

The dielectric response for the water, separating the membrane from the glass surface, is based on direct measurements of the spectral data of water and this approach is provided by Dagastine et al. [47]. The Kramers-Kronig relations were used for a direct integration to construct $\epsilon_{water}(\omega)$ based on the spectral data from the experiment. These data is provided by the authors in a table and a linear interpolation is used for frequencies in between. The values based on this data lie between the two older models by Parsegian and Weiss [52] and Roth and Lenhoff [53], therefore providing an excellent basis for the dielectric function of water.

BSA

The dielectric response for the BSA layer on the glass coverslip is given in a model by Eden et al. [54] that is based on steady state conductivity and polarization measurements. The measurements were used to determine ϵ_∞ and ϵ_s , i.e. the dielectric response for the

limiting high and low frequency. Then the α -dispersion is used for the generalized equation

$$\epsilon_{BSA}(\omega) = \epsilon_{\infty} + \frac{\epsilon_s - \epsilon_{\infty}}{(1 + (i\omega\tau)^{1-\alpha})^{\beta}},$$

with $\alpha = 0.48$, $\beta = 0.93$, relaxation time $\tau = 0.55$ s, and the frequency ω . This equation is used for the approximation of the BSA layer.

PEG 2000

The layer with PEG is a mixture of PEG and water and therefore we have to calculate the dielectric function for PEG and then combine it with the dielectric function for water [55]. The derivation for the PEG 2000 follows the same principle as Equation 12 for the glass with $\omega_{uv} = 1.87 \times 10^{16}$ rad/s, $\omega_{ir} = 2.11 \times 10^{14}$ rad/s, $C_{uv} = 1.0985$, and $C_{ir} = 37.9015$ as provided in a table in Masuda's Appendix A [51]. The addition for PEG is the surrounding water, and PEG only occupies a certain volume fraction v_{PEG} and water v_{water} , respectively. v_{PEG} is addressed by calculating the dielectric function of a heterogeneous mixture of water and PEG,

$$\epsilon_{(PEG-in-water)}(\omega) = \left((\epsilon_{PEG}(\omega))^{1/3} - (\epsilon_{water}(\omega))^{1/3} \right) v_{PEG} + (\epsilon_{water}(\omega))^{1/3} \Big)^3,$$

with ϵ_{PEG} the dielectric function for PEG and ϵ_{water} for water [56].

A different approach for the mixture of PEG and water is based on the Clausius-Mossotti mixture equation [57, 58],

$$\frac{\epsilon_{(PEG-in-water)}(\omega) - 1}{\epsilon_{(PEG-in-water)}(\omega) + 2} = v_{PEG} \frac{\epsilon_{PEG}(\omega) - 1}{\epsilon_{PEG}(\omega) + 2} + v_{water} \frac{\epsilon_{water}(\omega) - 1}{\epsilon_{water}(\omega) + 2},$$

which is also used to calculate $\epsilon_{(PEG-in-water)}$. Further analysis shows that the difference between the two approaches is negligible for our simulations and therefore we use the heterogeneous mixture in further steps.

The volume fraction of PEG is estimated by approximating the volume of one PEG molecule. The PEG 2000 molecule $C_{133}H_{267}N_2O_{55}P$ [59] is estimated by the volume of

the single atoms with their atom radius

$$V = \frac{4}{3}\pi (133 \cdot 70^3 + 267 \cdot 25^3 + 2 \cdot 65^3 + 55 \cdot 60^3 + 100^3) \text{ pm}^3 = 0.265 \text{ nm}^3.$$

Combined with the surface density of attached PEG on the membrane in an experiment, $3.6 \times 10^{16} \text{ m}^{-2}$ [25], this gives a volume fraction of 0.28% and thereby we have determined the dielectric properties of the water-PEG-mixture.

Membrane

The membrane used in the experiment by Monzel et al. [25] is a SOPC (1-stearoyl-2-oleoyl-sn-glycero-3-phosphocholine) membrane. For our implementation we had to simplify the structure by using a combination of choline, dihydrogen phosphate (H_2PO_4) and glycerol for the headgroup and hexadecane for the tailgroup. This simplification is justified as the dielectric properties of the materials are very similar. The next step is to combine these materials for the membrane and to calculate the dielectric function of the whole membrane. This combination is done by the use of the Clausius-Mossotti equation [60] which gives a relation between the polarizability of the molecules, the density of the material, and the dielectric function

$$\epsilon \approx 1 + 4\pi(\rho \cdot \alpha),$$

where α is the polarizability of the molecules and ρ is the density of the material. For the membrane this gives

$$\epsilon_{\text{membrane}} \approx 1 + 4\pi(\rho_{\text{Choline}} \cdot \alpha_{\text{Choline}} + \rho_{\text{H}_2\text{PO}_4} \cdot \alpha_{\text{H}_2\text{PO}_4} + \rho_{\text{Glycerol}} \cdot \alpha_{\text{Glycerol}}).$$

The density of each material is calculated for loose packing by an estimation of the surface area of each ion (A_{Ion}) and the depth of each Ion (d_{Ion})

$$\rho_{\text{Ion}} = \frac{1}{A_{\text{Ion}} \cdot d_{\text{Ion}}}.$$

The estimation of A_{Ion} is $(5 \times 10^{-3} \text{ nm})^2$ and the depth is 0.0268 nm for choline, 0.0226 nm for dihydrogen phosphate, and 0.0246 nm for glycerol. The polarizability for each fre-

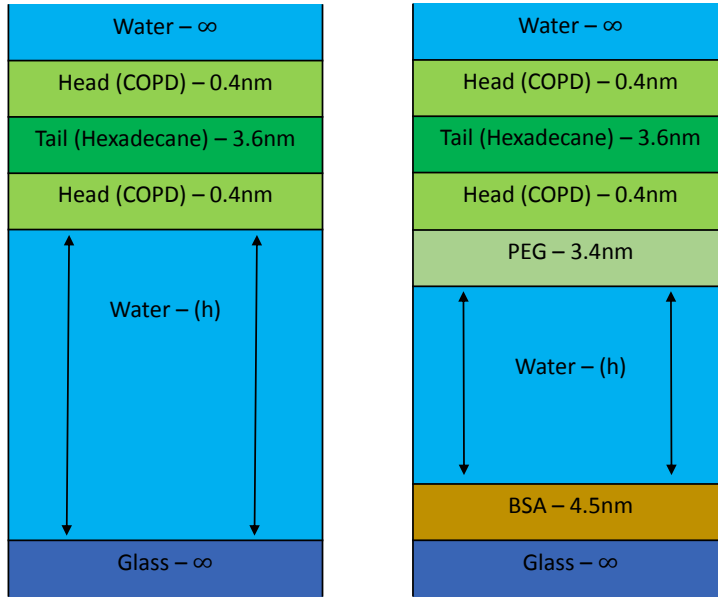


Figure 4: Two different implementations to simulate the experimental setup. The arrows show that water is the medium in which the height h is varied to figure out the Hamaker constant for different heights. Water and glass, as the limiting materials on top and bottom, are treated as semi-infinite.

quency is tabulated and comes from quantum mechanical calculations using MOLPRO [61,62] and TURBOMOLE [63].

The tailgroup is implemented with hexadecane as a substitute for the stearyl, because it has roughly the same length and molecule structure. The implementation of hexadecane follows Masuda et al. [51] and Equation 12 with $\omega_{uv} = 1.84 \times 10^{16}$ rad/s, $\omega_{ir} = 5.51 \times 10^{14}$ rad/s, $C_{uv} = 1.0244$, and $C_{ir} = 0.0256$. This completes all material properties for the membrane used in the experiment.

2.2.2 Complete Setup

Having defined the dielectric properties for all materials in use, we can look at the complete setup: BSA coated coverslip, water, PEG coated membrane floating in the

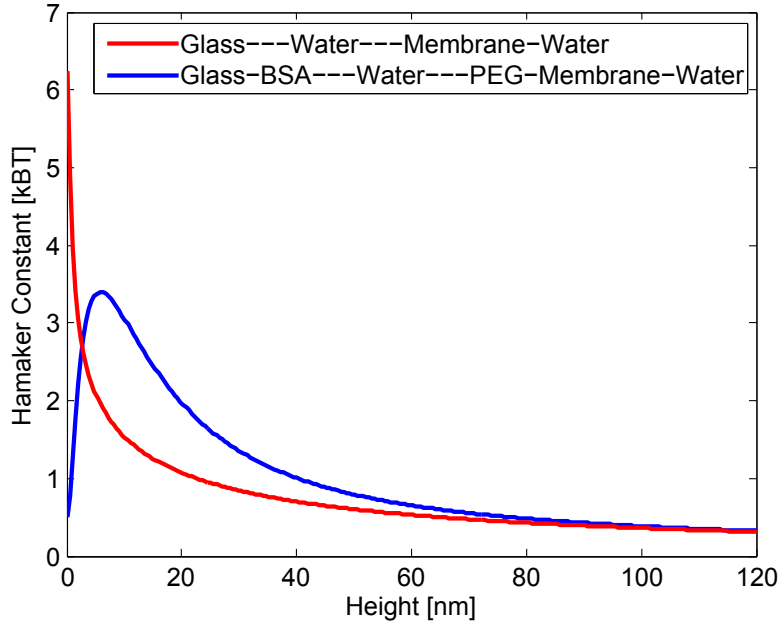


Figure 5: Resulting Hamaker Constant for the two systems.

water. To judge whether the coating with BSA and the PEG on the membrane have a relevant influence on the resulting van der Waals interaction, we compared the system with and without coating. Figure 4 shows both systems in comparison and gives details on the dimensions. The semi-infinite height of the limiting glass and water is justified, as the dimensions of glass and the water in the vesicle exceed other dimensions in the system by far.

2.3 Results and Discussion

First, we have a look at the Hamaker constant from the simulation. Figure 5 shows the Hamaker constant plotted against the thickness of the water layer between glass and membrane, i.e. the height of the membrane. For the uncoated system this gives a Hamaker constant of about $6 k_B T$ for small heights and a decline to $0.4 k_B T$ for rising heights. The decline flattens out for higher distances and a fit with an algebraic function

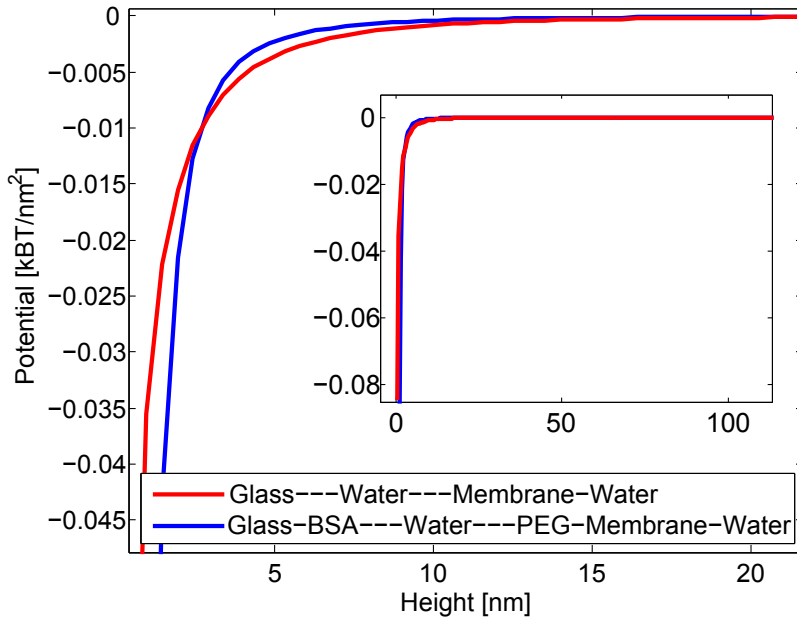


Figure 6: Resulting potential for both systems. The inset shows the whole range from 0 to 100nm

remains elusive. The Hamaker constant for the system with BSA and PEG has a similar behavior from about 6 nm on, while also flattening out at about $0.4 k_B T$, but here the Hamaker constant also declines for very small distances. This creates a maximum of the Hamaker constant off $3.4 k_B T$ at 6 nm. Linear extension to zero gives $0.5 k_B T$ for 0 nm.

Given the Hamaker constant for each height, we calculate the corresponding potential using

$$V_{vdW} = -\frac{1}{12\pi} \frac{A_H(h)}{h^2}.$$

This results in the distribution shown in Figure 6. Key of the shape is the $\frac{1}{h^2}$ term of the potential with the changing Hamaker constant as prefactor, which implies the following: the potential for the coated system flattens out more quickly for higher distances and at the same time diverges faster for small heights. Both potentials intersect at 2.7 nm where they have the same Hamaker constant. On the larger scale of 0 nm to 100 nm, as

shown in the inset of Figure 6, the two potentials have a very similar shape.

For further simulations with the van der Waals potential, a good fit is required to avoid using interpolated points. With the non-algebraic behavior of the Hamaker constant, this turns out rather challenging and so we had a closer look at three different candidates. The simplest form is

$$V_{vdW}(h) = -\frac{A_H}{12\pi} \frac{1}{h^2} \quad (13)$$

that describes the van der Waals interaction for two half spaces. In combination with the exact Hamaker constant $A_H(h)$, this gives the exact potential. But, when used as a fit for the whole potential, A_H is kept constant. It is obvious that with a height dependent Hamaker constant this is not a very good fit, but it sets a basis for the comparison with more elaborate fits.

One of which,

$$V_{vdW}(h) = -\frac{A_H}{12\pi} \left(\frac{1}{h^2} - \frac{1}{(h+d)^2} \right), \quad (14)$$

was introduced by Parsegian [44] for a system with glass, buffer, membrane, and sucrose solution. By including the thickness of the membrane d , Equation 14 takes into account that the membrane is only a thin layer in water, but still doesn't account for BSA on the glass or PEG on the membrane.

Lipowsky [64] takes into account that aqueous solution in biological systems is usually 'salty' and with that the screening length for the zero-frequency part of the van der Waals interaction is of the order of 1 nm. This results in

$$V_{vdW}(h) = -\frac{A_H}{12\pi} \left(\frac{1}{h^2} - \frac{2}{(h+d)^2} + \frac{1}{(h+2d)^2} \right) \quad (15)$$

for the description of the potential. Despite the fact that Equations 14 and 15 include the membrane thickness as a second parameter, only the Hamaker constant A_H was used as a fitting parameter. The membrane thickness d is kept constant at 4 nm, which is roughly the thickness of the membrane in an experimental setup. In the system with PEG coating d is also kept at 4 nm, because the low volume fraction of the PEG makes

Table 2: Hamaker Fits and Their Qualities.

The van der Waals potential diverges at zero, which is prone to errors when it comes to fitting. Therefore we vary the height h_0 , from which on the fit is performed upwards. A_H is the Hamaker constant from the fitting and the r^2 -error gives a measure for the fit quality, which is explained in detail in the paragraph below.

	Glass — Water — Membrane - Water								
Fitttype	Equation 13			Equation 14			Equation 15		
$h_0[\text{nm}]$	0.97	6.76	13.98	0.97	6.76	13.98	0.97	6.76	13.98
$A_H[\text{k}_B\text{T}]$	3.76	1.62	1.11	3.98	3.10	3.42	4.14	4.78	7.62
r^2 -error	0.990	0.978	0.968	0.996	0.999	0.998	0.998	0.982	0.966

this layer more water-like than membrane-like in the Lifshitz calculation and therefore doesn't contribute to the membrane thickness.

According to Rädler et al. [65], we can expect a Hamaker constant of approximately $1 \text{ k}_B\text{T} - 4 \text{ k}_B\text{T}$ for biological material in water while referring to Equation 14. Having defined the different fit for Equations 13, 14, 15 and a rough frame on which Hamaker constant to expect, we have a closer look at the results for fitting the Lifshitz calculations.

Table 2 and 3 show the resulting Hamaker constant A_H in k_BT and the corresponding error depending on the height h_0 at which the fit started. The different h_0 basically describe how much the divergence at zero height is taken into account and where we achieve the highest accuracy. High h_0 means higher accuracy for the potential further away from zero and a smaller h_0 takes the potential at closer distances into account. The error as a measure for the fit quality is the r^2 -error, which is implemented in the Curve Fitting Toolbox in Matlab [66]. The r^2 -error gives a measure on how much of the variation of the data is described by the fit: a value between zero and one is possible and this corresponds to 0% to 100% of the total variation in the data about the average.

Table 3: Hamaker Fits and Their Qualities.

(For a description of h_0 , A_H , and r^2 -error see Table 2)

	Glass - BSA — Water — PEG - Membrane - Water								
Fittype	Equation 13			Equation 14			Equation 15		
h_0 [nm]	0.97	6.76	13.98	0.97	6.76	13.98	0.97	6.76	13.98
A_H [k _B T]	1.46	3.09	2.07	1.52	5.90	6.46	1.56	9.10	14.50
r^2 -error	0.930	0.980	0.942	0.908	0.997	1.000	0.894	0.977	0.986

The mathematical definition is the ratio of the squares of regression (SSR)

$$SSR = \sum_{i=1}^n w_i (\hat{y}_i - \bar{y})^2$$

and the total sum of squares about the mean (SST)

$$SST = \sum_{i=1}^n w_i (y_i - \bar{y})^2$$

resulting in r^2 -error = $\frac{SSR}{SST}$. So basically the ratio of the squared gaps between regression and mean and the squared gaps between the actual values and mean.

The uncoated system with glass, water, membrane, and water is shown in Table 2. According to the r^2 -error the fit using Equation 14 is the best fit for the overall system. Only Equation 15 is slightly better when including most of the divergence from 0.97 nm on. As expected Equation 13 is the worst fit overall as it is the most simple approach, which completely ignores the height dependence of the Hamaker constant. The resulting Hamaker constants for this system lies at about 3.5 k_BT for Equation 14, is lower for Equation 13 with about 1.5 k_BT for higher distances and about 4.5 k_BT for Equation 15.

Including BSA on the glass and PEG on the membrane we can analyze a more experimentally realistic and sophisticated system. Table 3 shows that on average all three fits perform worse for the coated system. As the coated system is more complicated, and therefore further away from the theoretical basis on which the fits are based, this

seems reasonable. While the performance is still poor for low distances, Equation 14 performs very well for heights above 7 nm and perfect for distances above 14 nm. With the Hamaker constant at about $6 k_B T$ this is higher than expected and a bit above the frame provided by Rädler [65].

Combining both results we can conclude that the best fit for the given system is provided by Equation 14 in accordance with [25]. The resulting Hamaker constant for the uncoated system is within the expected range for biological systems, while the more realistic system differs from that frame. Across both systems it is noticeable that the Hamaker constant varies with different definitions for the van der Waals potential and different starting heights h_0 for the fit. In order to analyze a system close to the experimental reality, it is necessary to either choose the form of the potential very carefully for the regarded height or to incorporate the height dependence of the Hamaker constant into the system.

For the following analysis of the behavior of a fluctuating membrane in an external potential, we take a step back and first focus on a van der Waals potential described by $\propto \frac{1}{h^2}$ for simplicity and to avoid unnecessary many parameters. After getting the basics of the fluctuating membrane right in this system, we expand the whole simulation for a more realistic experimental setup with the appropriate van der Waals potential.

3 Effective Membrane Substrate Potential

Having addressed the details of the external Hamaker potential, the next step is to incorporate the membrane fluctuations into the model. This allows to round out the system by having the fluctuating membrane and the external potential combined. This system is implemented as Monte Carlo simulation [67–70].

3.1 Method: Monte Carlo Simulations

For the Monte Carlo simulations the membrane is described as a square lattice with a given height for each lattice point, basically a discretized Monge representation. In this approach, the energy of the membrane is only dependent on the height of each lattice point and its neighbors, and therefore the system is fully described by a square lattice of heights.

The first step in the simulation is to determine the energy of the membrane profile in order to calculate the acceptance probability for new Monte Carlo steps. The membrane’s energy is described by the external potential V_{pot} and its bending energy E_B that is described by the Monge representation (cf. Equation 3) [69]

$$E = E_B + V_{pot} = \frac{\kappa}{2} \int d^2r [\nabla^2 h(r)]^2 + V_{pot}, \quad (16)$$

which is valid for nearly planar fluid membranes. Hereby $h(r)$ represents the vertical height difference between membrane and planar surface (i.e. glass), κ the bending rigidity of the membrane, r the position on the membrane, and V_{pot} represents external potentials. The membrane is discretized in h on a $64 \cdot 64$ square lattice as $h_{x,y}$ with lattice constant a and periodic boundary conditions. In the Monge representation this reads

$$E \approx \sum_{x,y} \left\{ \frac{\kappa}{2a^2} (h_{x+1,y} + h_{x-1,y} + h_{x,y+1} + h_{x,y-1} - 4h_{x,y})^2 + V_{pot}(h_{x,y}) \right\}. \quad (17)$$

In Equation 17, we use the standard discretization of the Laplace operator for a discretized membrane shape $h_{x,y}$.

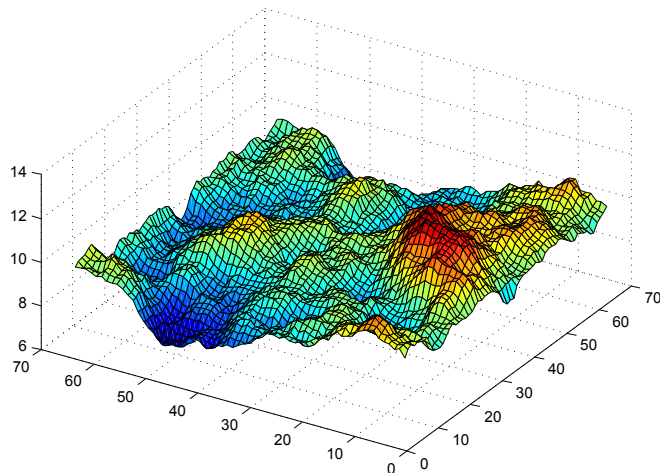


Figure 7: Example of a membrane provided by Monte Carlo simulations.

Having determined how the membrane's energy is treated in our simulation, we have to address the issue of random numbers for the step sizes, the choice of grid point, and for the acceptance test in the Monte Carlo step. The random number generator in use is provided in the GNU Scientific Library [71] and is based on the CRAY MATHLIB routine RANF. The period of this generator is 2^{46} which is large enough for long simulations. If not stated otherwise the simulations run for 12×10^9 steps which is three orders of magnitude smaller than the period of the random number generator in use. One grid point (x, y) is then chosen by use of random numbers for the height modification. $h_{x,y}$ is changed by a random height $\pm\Delta h$, uniformly distributed between -2 nm and 2 nm.

With given position (x, y) and step size Δh , the energy is calculated for $h_{x,y}$ and its neighbors according to Equation 17. The difference of the new energy after the random step Δh and the previous energy are then compared. The step is accepted immediately if it is energetically favorable, otherwise $e^{-\frac{\Delta E}{k_B T}}$ is compared to a random number between 0 and 1 and only accepted if larger. This avoids that the membrane gets trapped in a minimum that is not the global minimum. The step size was chosen as such, that the acceptance rate is between 40% and 60%.

A further issue that has to be addressed is the storage of the height profiles. During

the simulation it is necessary to keep a $64 \cdot 64$ array with double precision for the height profiles as interaction with neighboring points is relevant. For the evaluation of the results only the height profile for h without point specification x, y is relevant. Therefore, a histogram from 0 nm to 100 nm that stores the height of every step in 400 bins with a width of 0.25 nm each is implemented. This histogram is then saved every 1×10^9 th step and twelve times for every run. While this histogram method only provides an accuracy of 0.25 nm and doesn't incorporate an exact map, it enables us to include every single step in the final distribution. This wouldn't be possible by saving the height array itself. This solution, combining a height array during runtime and a histogram for the analysis, is the best compromise of accuracy, analyzability and processing time.

To evaluate our simulation we implemented systems that can be solved analytically, such as the membrane in a harmonic potential, or were analyzed in great detail before, such as the Helfrich repulsion between membrane and impermeable wall.

3.1.1 Validation with Harmonic Potential

The analytical result for a membrane fluctuating in a harmonic potential is used to validate the variance of the membrane fluctuations in the implementation. V_{pot} describes the harmonic potential by $V_{pot}(h) = \frac{\gamma}{2}(h - h_0)^2$. The relation between the strength of the harmonic potential γ and the variance of the fluctuating membrane $\langle \Delta h^2 \rangle$, that can be measured numerically, is given by

$$\langle \Delta h^2 \rangle = \frac{k_B T}{8\sqrt{\kappa\gamma}}. \quad (18)$$

Equation 18 can be derived by analyzing the Monge representation in Fourier Space [72]. By simulating fluctuating membranes in various harmonic potentials and measuring the variance, we were able to come to an excellent agreement with the analytical result as shown in Figure 8. All red crosses are on the line for the analytical result and by that reproduce the law relating variance and γ . The combination of Equation 18 and Figure 8 gives proof that the bending energy is implemented in our simulation in a correct way.

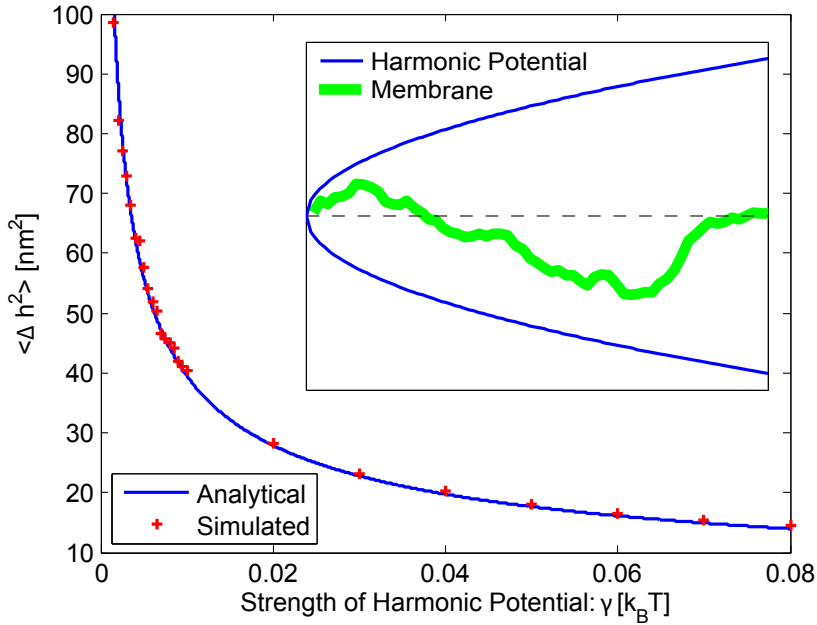


Figure 8: Variance of the membrane plotted against the strength of the harmonic potential and the analytical solution $\langle \Delta h^2 \rangle = \frac{k_B T}{8\sqrt{\kappa\gamma}}$ (no fit parameter). The inset shows an example of a membrane fluctuating in the harmonic potential.

3.1.2 Validation with Helfrich Repulsion

To make sure that also the interaction with a hard wall, described by Helfrich repulsion, is implemented properly we exert pressure p on a membrane to push it close to an impermeable wall

$$V_{pot}(h) = p \cdot h.$$

The wall is implemented as such that any step that would lead into the wall is not accepted. This means that there is no reflection or anything similar in the implementation, just a prohibition from entering the wall. The membrane then sits in the equilibrium between Helfrich repulsion and pressure. This exact system has been analyzed by Weikl and Lipowsky [64, 73] in great detail and the result (also by Monte Carlo simulations) is

given by

$$p = 2c \frac{(\text{k}_B\text{T})^2}{\kappa} h^{-3}$$

with $2c = 0.115 \pm 0.005$. Figure 9 shows the results from our simulation including the fit

$$h(p) = \left(\frac{\kappa}{2c(\text{k}_B\text{T})^2} \right)^{-\frac{1}{3}} \cdot p^{-\frac{1}{3}} = b \cdot p^{-\frac{1}{3}} \quad (19)$$

with $b = \left(\frac{2c(\text{k}_B\text{T})^2}{\kappa} \right)^{\frac{1}{3}}$. After Weikl and Lipowsky, this gives $b = 0.4863 \pm 0.1710$, $b = 0.2257 \pm 0.0794$, and $b = 0.1048 \pm 0.0368$ for $\kappa = 1 \text{ k}_B\text{T}$, $\kappa = 10 \text{ k}_B\text{T}$, and $\kappa = 100 \text{ k}_B\text{T}$ respectively. The fit from our simulations is in perfect agreement with Weikl and Lipowsky ($b = 0.477$, $b = 0.228$, $b = 0.102$, see Figure 9).

Combining the results from Chapters 3.1.1 and 3.1.2 we can conclude that the simulation framework is valid for simulating membranes in external potentials, including the interaction with an impermeable wall. At this point one further remark on the impermeable wall has to be made: treating the wall by discarding new steps that would enter the wall can lead to numerical errors. A non-linear force pressuring the membrane against the wall suppresses new simulation steps. This causes the membrane to get stuck or glued to the wall and the acceptance rate of the simulation to decline. To avoid this numerical error we implement the wall by a very steep repulsive potential in a very similar manner as the treatment of the PEG layer.

3.1.3 Finding a Proper External Potential

Due to numerical difficulties we have to treat the impermeable wall, i.e. the glass, as a very steep repulsive potential. This potential can be evaluated in great detail, including the surface roughness and various material properties, as done by Parsons et al. [74]. At this point we follow a more simple approach that goes along with the description of the PEG layer between membrane and glass. For the repulsive potential a diverging term like $\frac{1}{h^2}$ stands to reason and also a damping like e^{-h^2} to avoid influence further away from the interaction is necessary.

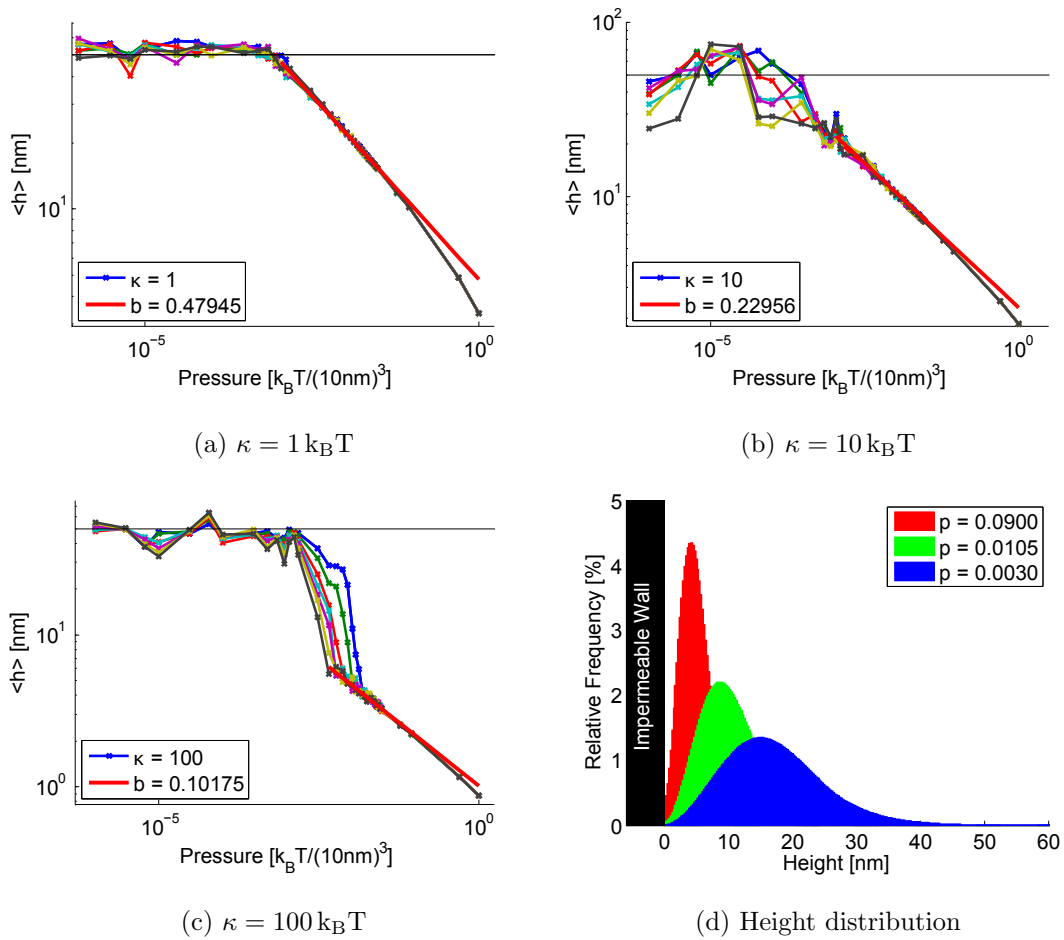


Figure 9: (a) to (c): Average height of the membrane plotted against the external pressure put on the membrane. The trend is fitted with Equation 19.

(d): Three examples of the membrane height distribution (histogram) when pressed against the impermeable wall for $\kappa = 10 \text{ k}_B T$.

Bruinsma et al. [18] provide a description for the interaction when PEG is between two surfaces (cf. Equation 4)

$$V_{PEG}(h) = \frac{\pi^2}{6} k_B T \rho_{PEG} \left(\frac{r_{PEG}}{h} \right)^2 e^{-\frac{3}{2} \left(\frac{h}{r_{PEG}} \right)^2}. \quad (20)$$

Equation 20 also contains both the $\frac{1}{h^2}$ and e^{-h^2} term, modified to account for a given PEG radius. Hereby r_{PEG} is the radius of the PEG molecules, ρ_{PEG} is the density of the PEG molecules on the surface and h is the current height.

To keep the number of parameters low and the description of the system as simple as possible, we adjust Equation 20 to a more general form

$$V_{mat}(h) = \frac{\pi^2}{6} k_B T \rho_{mat} \left(\frac{r_{mat}}{h} \right)^2 e^{-\frac{3}{2} \left(\frac{h}{r_{mat}} \right)^2}, \quad (21)$$

with r_{mat} the radius of the roughness of the surface and ρ_{mat} the density of the material. For instance for a surface of glass r_{mat} is expected to be about 0.5 nm, with ρ_{mat} about 1 nm^{-2} , while PEG can be described by 3.4 nm and $3.62 \times 10^{-2} \text{ nm}^{-2}$ [25], respectively.

In combination with Equation 21, we use the simplest form (cf. Equation 13) for the van der Waals potential and the fluctuating energy to get to the full energy

$$E = \sum_{x,y} \left[\frac{\kappa}{2a^2} (h_{x+1,y} + h_{x-1,y} + h_{x,y+1} + h_{x,y-1} - 4h_{x,y})^2 - \frac{A_H}{12\pi} \frac{1}{h_{x,y}^2} + \frac{\pi^2}{6} k_B T \rho_{mat} \left(\frac{r_{mat}}{h_{x,y}} \right)^2 e^{-\frac{3}{2} \left(\frac{h_{x,y}}{r_{mat}} \right)^2} \right]. \quad (22)$$

Equation 22 completes the setup for the Monte Carlo simulation and allows us to analyze the behavior for different parameters. To illustrate how the parameters influence the external potential, two different sets are shown in Figure 10. It is obvious that, with a smaller radius for the repulsion, the influence of the diverging van der Waals potential gains importance. Additionally the minimum gets deeper and more narrow for the short range repulsive behavior. As the description for the van der Waals interaction in Equation 13 and the repulsive potential in Equation 21 is rather crude, we had a closer look at a whole range of parameters. The broad range of parameters also serves the

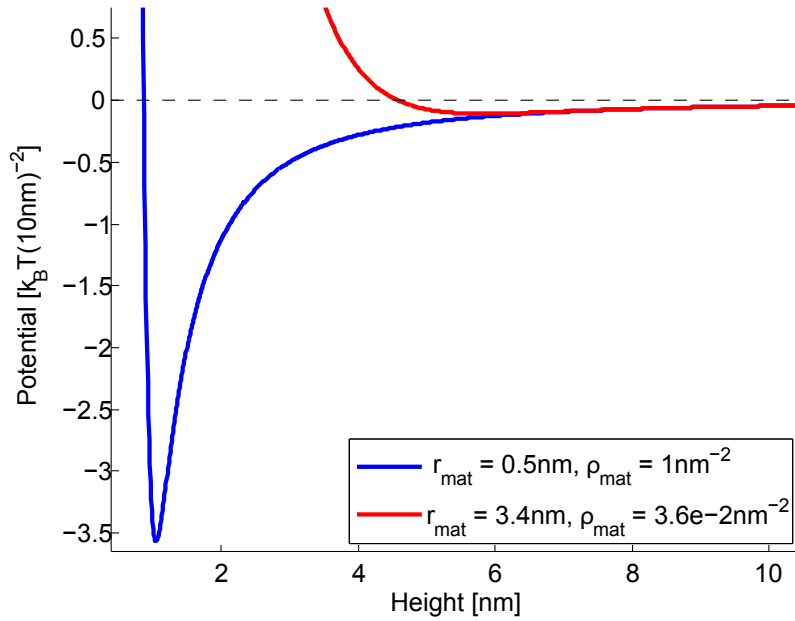


Figure 10: Two examples for external potentials with different parameters, the blue curve would be suitable for glass and the red curve for PEG on the glass. $A_{Ham} = 1.69 k_B T$ in both cases.

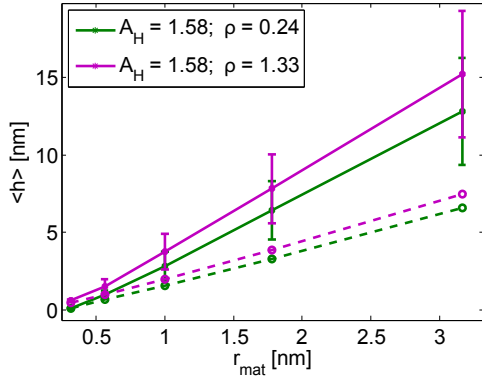
fact that the determination of the exact parameters for an experiment, like the Hamaker constant or height of the PEG layer, is difficult.

3.2 Results

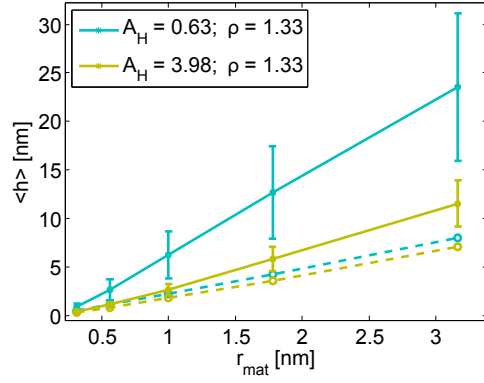
We performed simulations using the Monte Carlo framework introduced in Chapter 3.1 and Equation 21 to gain further insight on the behavior of the fluctuating membrane. To take the system with and without PEG and BSA into account, the implementation involves two sets of material radius and density. First a material radius of 0.3 nm to 3.2 nm and densities from 0.24 nm^{-2} to 1.33 nm^{-2} are used to account for the glass surface. These large ranges are chosen as such to include glass with a rough and smooth surface. For the system that includes PEG or/and BSA the radius varies from 1.6 nm

to 16.0 nm with a density from $3 \times 10^{-2} \text{ nm}^{-2}$ to $3 \times 10^{-1} \text{ nm}^{-2}$. This broad range of radii and densities includes estimations for PEG only, BSA only and the combination of both. All simulations run for 12×10^9 Monte Carlo steps, so that on average every point x, y in the height profile $h_{x,y}$ made 3×10^6 steps with an acceptance rate between 40% and 60%. All data points start at a distance of 10 nm from the surface. Figure 11 shows the results for different systems and compares the result from the simulation with the result from taking the minimum of the external potential. Figure 11 (a) and (b) show the simulation results for glass. For short r_{mat} , the simulation result is within one standard deviation of the result calculated as the minimum of the external potential. For a higher material radius, this is no longer true and the membrane mean sits up to two standard deviations away from the calculated minimum. It is worth remarking that with rising r_{mat} , the mean height $\langle h \rangle$ rises linearly for the expected values of the calculation and for the simulation as well. Figure 11 (a) shows the effect of variation of the material density on the behavior: with a higher density for the glass the estimated and the simulated mean are further away from the surface. The difference between the simulated heights for the two parameters is about twice to thrice as big as the difference between the calculated heights. Figure 11 (b) shows the effect of the variation of the Hamaker constant. Thereby, the difference between the simulated heights is at least one order of magnitude bigger than the difference for the expected heights. This shows that for the correct analysis of experimental results a detailed knowledge of the exact Hamaker constant is required.

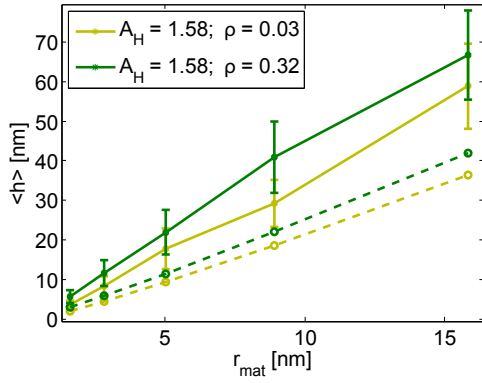
Simulation results for a system with BSA and PEG coating are shown in Figure 11 (c) and (d). The variation of the density of the coatings in (c) shows about the same effect as the variation of the density for the glass: The difference between the simulated values is about two or three times larger than the difference between the expected heights. For the variation of A_H in (d) the same effect as in (b) is visible. The height difference for the simulated results is vastly bigger than the height difference for the calculated



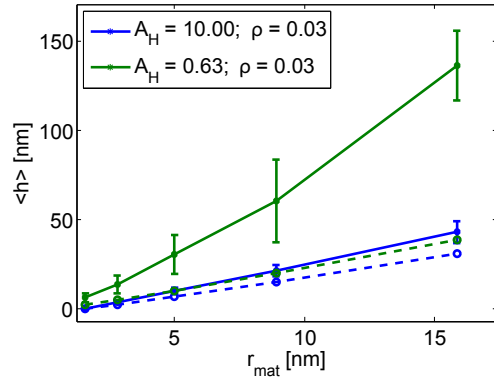
(a) Glass - varying ρ



(b) Glass - varying A_H



(c) PEG/BSA - varying ρ



(d) PEG/BSA - varying A_H

Figure 11: Different results for $\kappa = 10 \text{ k}_B\text{T}$. (a) and (b) describe a system with glass and membrane that is not coated, (c) and (d) correspond to a system with either PEG, BSA or both. The errorbars show the standard deviation in nm and hence also give a measure for the membrane fluctuations. The unit for A_H is k_BT and for ρ it's nm^{-2} . The simulation for (d) with $A_H = 0.63 \text{ k}_B\text{T}$ was running with 250×10^9 timesteps to ensure convergence with a starting height of 10 nm and a very flat potential.

results. The increased amount of timesteps for the simulation with $A_H = 0.63 \text{ k}_B\text{T}$ is necessary because of the start at 10 nm and the external potential being very flat with these parameters.

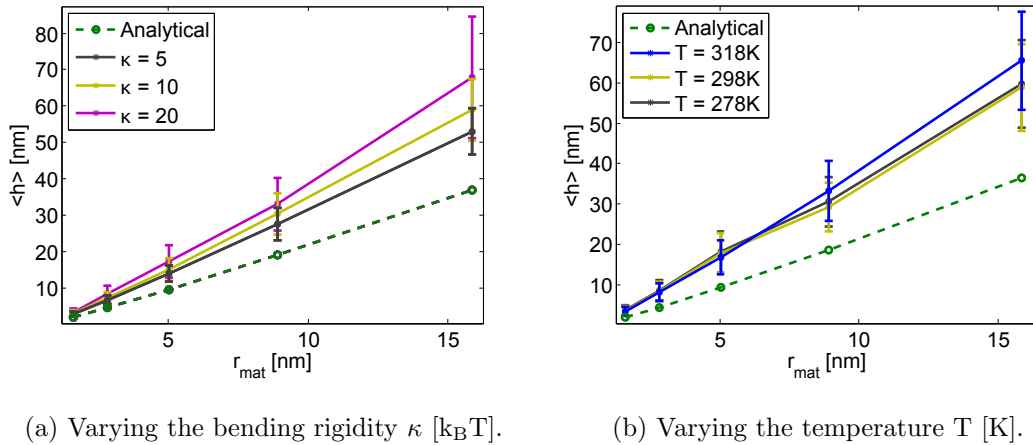


Figure 12: Analysis of the influence of bending rigidity κ and temperature on the average membrane height $\langle h \rangle$. The remaining parameters for these plots are $A_H = 1.58 \text{ k}_B\text{T}$ and $\rho = 0.03 \text{ nm}^{-2}$.

A further parameter to analyze is the influence of the membrane's bending rigidity. The bending rigidity is a measure for the bending stiffness and therefore a parameter that is related to the strength of the repulsive Helfrich force. Figure 12 (a) shows the behavior of a membrane with $\kappa = 5 \text{ k}_B\text{T}$, $\kappa = 10 \text{ k}_B\text{T}$ and $\kappa = 20 \text{ k}_B\text{T}$. The result shows that higher bending rigidity means higher $\langle h \rangle$ for the membrane. This relation was expected as the bending rigidity only increases the fluctuations and therefore the repulsive part of the interaction. A detailed analysis of the correct bending rigidity for the comparison with experimental results is provided in Chapter 3.3.

We also analyzed the influence of temperature on the system. Hereby, we note that we didn't change the value for κ or A_H , as they have a rather complicated temperature dependence. The temperature dependence of κ or A_H would only lead to a different value for the parameter and this effect was already analyzed earlier in this chapter. Hence,

the change in temperature only influences the decision whether a new Monte Carlo step is accepted or not, i.e. a higher chance for higher temperature and a lower chance for low temperature. It follows that a higher temperature only allows more fluctuations in the external potential. The result is shown in Figure 12 (b). The simulation with 318 K is further away from the surface for larger r_{mat} , but the overall influence seems rather small. Simulations with temperatures that differ in one order of magnitude or more confirm the result that higher temperature means further away from the surface, but from a biological and physical point of view it doesn't make much sense to look at membranes in water for a temperature higher than 318 K or lower than 278 K.

As a summary, we conclude that higher bending rigidity κ , material radius r_{mat} , material density ρ_{mat} , and temperature lead to higher distances between fluctuating membrane and surface. These are also the parameters that we need to adjust to set up a simulation to understand experimental results.

3.3 Can we Reproduce Experiments?

After identifying the influence of various parameters on the membrane height we want to address the reproducibility of experimental results with our simulation. The basis for the experimental results are measurements by Monzel et al. using RICM measurements [25]. The membrane in the experiment is a SOPC membrane with PEG-2000 on the membrane and a BSA layer on the glass. The experiments reveal that the average height of the membrane is $80 \text{ nm} \pm 8 \text{ nm}$. The next step is to have a closer look at the necessary potentials to simulate this setup.

The van der Waals potential was analyzed in great detail in Section 2. The best fit for the van der Waals interaction of this setup is provided by

$$V_{vdW}(h) = -\frac{A_H}{12\pi} \left(\frac{1}{h^2} - \frac{1}{(h+d)^2} \right).$$

We expect the membrane to rest at rather large distances, so we used a Hamaker constant of $6.5 k_B T$, which is the best fit for distances above 14 nm as shown in Table 3. To

analyze the importance of the value of the Hamaker constant, we also ran simulations with $A_H = 1.5 \text{ k}_B\text{T}$ and $A_H = 3.0 \text{ k}_B\text{T}$. The Hamaker constant and the form of the van der Waals potential give the basis for the attractive part of the potential. The repulsive part of the external potential is implemented by

$$V_{mat}(h) = \frac{\pi^2}{6} k_B T \rho_{mat} \left(\frac{r_{mat}}{h} \right)^2 e^{-\frac{3}{2} \left(\frac{h}{r_{mat}} \right)^2}$$

as introduced in Chapter 3.1.3. The radius r_{mat} is the sum of the radius for r_{PEG} and r_{BSA} . r_{PEG} is given as 3.4 nm [25], but also higher radii of $15 \text{ nm} \pm 5 \text{ nm}$ for different PEG regimes were received in experiments [75–78]. This gap is taken into account by performing multiple simulations with different PEG sizes. The density of the PEG is $3.6 \times 10^{16} \text{ m}^{-2}$ [25]. The BSA coating in the experimental setup has a height of 4.5 nm. The density of the BSA is not provided for the experimental setup, but it is at least as dense as the PEG, and usually it's much denser than the PEG. In conclusion we ran our simulations with three different densities $4 \times 10^{16} \text{ m}^{-2}$, $10 \times 10^{16} \text{ m}^{-2}$, and $35 \times 10^{16} \text{ m}^{-2}$, the first slightly above the PEG density, the second about twice as big, and the third one order of magnitude larger.

For the reproduction of experimental results with SOPC, we need to work with the correct bending rigidity. Previous studies by Evans et al. [79] provided a value of $21.9 \text{ k}_B\text{T} \pm 1.46 \text{ k}_B\text{T}$ for SOPC by analyzing the relation between tension and projected surface area through experimental sensitive micropipet methods. For other membranes, such as DAPC, DGDG, and DMPC, the value was approximately 45% lower and for SOPC:CHOL around 273% higher. Zhou et al. confirmed the bending rigidity of $21.9 \text{ k}_B\text{T}$ for SOPC by the use of dynamic tension spectroscopy. Approximately $20 \text{ k}_B\text{T}$ bending rigidity is also provided by Hung et al. by micropipette aspiration [80]. We conclude that $20 \text{ k}_B\text{T}$ is the bending rigidity of choice for the simulation of SOPC.

With the last three paragraphs we have set all parameters, van der Waals potential and Hamaker constant, radius and density of PEG/BSA layer, and bending rigidity for a setup to reproduce experimental data. The Monte Carlo setup follows the exact same

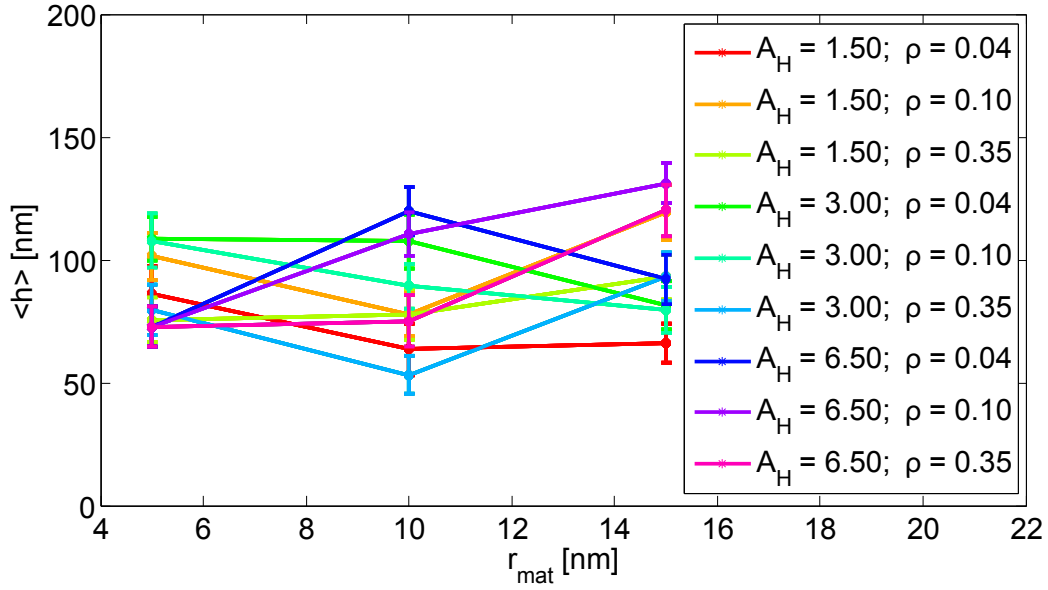


Figure 13: Results of a run with experimental setup parameters. The bending rigidity is $20 k_B T$, the unit for A_H is $k_B T$ and for ρ it's nm^{-2}

framework as provided in Chapter 3.1, with the exception that we used ten times more timesteps (12×10^{10}) to ensure convergence. Figure 13 shows the results of the simulation for all parameters. We see that all simulations give mean membrane heights between about 60 nm and 120 nm with a standard deviation of about 10 nm. Figure 13 also shows that there is no systematic influence of the simulation parameters in this setup. There is neither a direct influence of the material radius, nor of the material density or Hamaker constant. This phenomenon suggests that the value of the parameters is no guarantee to receive a certain height profile. Some experiments show the same phenomenon by giving different results for two runs, despite the exact same preparation. Overall the result is in the right order of magnitude for an experimental height of $80 \text{ nm} \pm 8 \text{ nm}$. Without bending any parameters, such as the Helfrich prefactor, this is an unprecedented result.

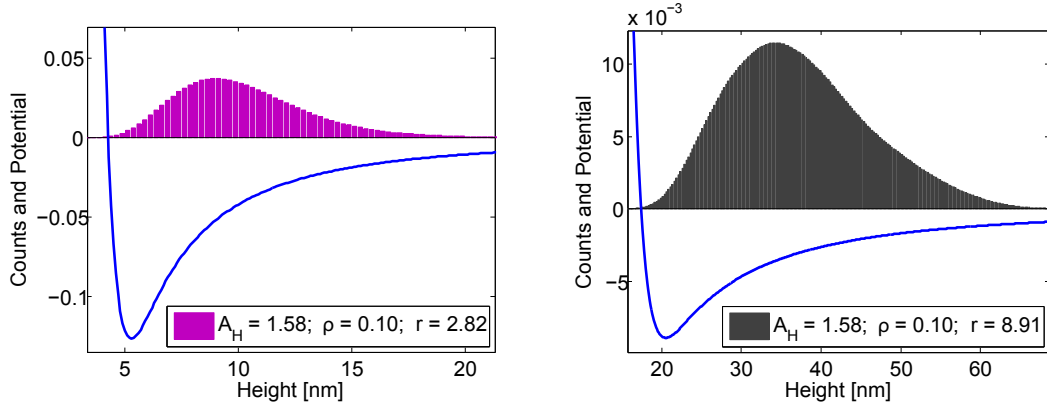


Figure 14: Height distribution for the membrane in the external potential. The number of counts is normalized and the plot of the external potential is scaled to fit into the figure. The unit for A_H is $k_B T$, for ρ it's nm^{-2} , and for r it's nm.

4 Conclusions: Helfrich Repulsion and Additivity

All the results in Chapter 3.2 were only compared to the minimum of the external potential of van der Waals and PEG repulsion combined, while the Helfrich potential was left aside. This was done due to the complications with additivity and to avoid too many parameters. In this chapter we will address the issue of the influence of the Helfrich potential. Figure 14 illustrates the distribution of the heights for a membrane in the external potential. The height distribution in Figure 14 shows that the contact of the fluctuating membrane with the divergence of the repulsive potential is one condition for the membrane's position. The length of the tail of the fluctuations determines how close the membrane can get to the divergence of the potential. The external potential also seems to influence the length of the fluctuation's tail. The tail on the left of the membrane is shorter, i.e. the distribution is more narrow, while the tail on the right side is rather flat and long. The effect of the suppression of the membrane fluctuations by the external potential is described by the Helfrich potential.

The Helfrich potential has the form of

$$V_H(h) = c_1 \frac{(k_B T)^2}{\kappa} \frac{1}{h^2}$$

as introduced in Chapter 1.2 and therefore gives a repulsive potential [39]. The basis for the Helfrich repulsion is the suppression of the membrane fluctuations by a hard wall, or in our case a strong repulsive potential. Looking at the experimental setup we have to deal with a membrane with attached PEG that sits on the membrane and therefore extends the suppression of the fluctuation. Hence a transformation $h \rightarrow (h - r_{mat})$ for $V_H(h)$ makes sense. The influence of this change is shown in Figure 15. First we

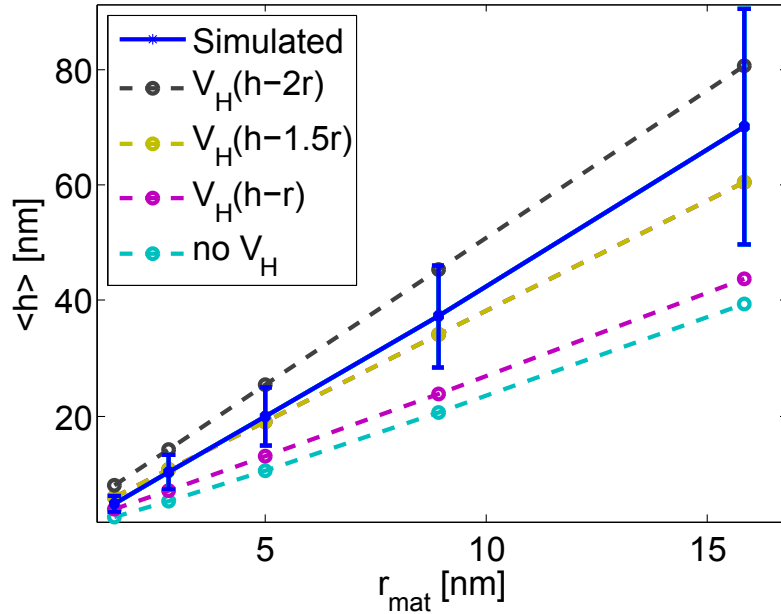


Figure 15: Minima of the external potential $V(h) = V_{vdW}(h) + V_{mat}(h) + V_H(h - r_{mat})$ for different displacements of the Helfrich potential and different r_{mat} . Further parameters: $A_H = 1.58 k_B T$, $\rho = 0.1 \text{ nm}^{-2}$.

had a closer look at $V_H(h - r_{mat})$ and realized that this increases the height of the minimum only slightly. This is due to the fact that the repulsive potential V_{mat} diverges already for slightly higher distances than $V_H(h - r_{mat})$ and therefore is the main repulsive

contribution. Adding more displacement to the Helfrich potential, like $h - 1.5r_{mat}$ or $h - 2r_{mat}$, gets the minimum closer to the simulated results but never really aligns properly for different r_{mat} . Therefore we conclude that an approach by just adding up all the potentials doesn't suffice for this problem and a different approach for the effective potential is yet to be found.

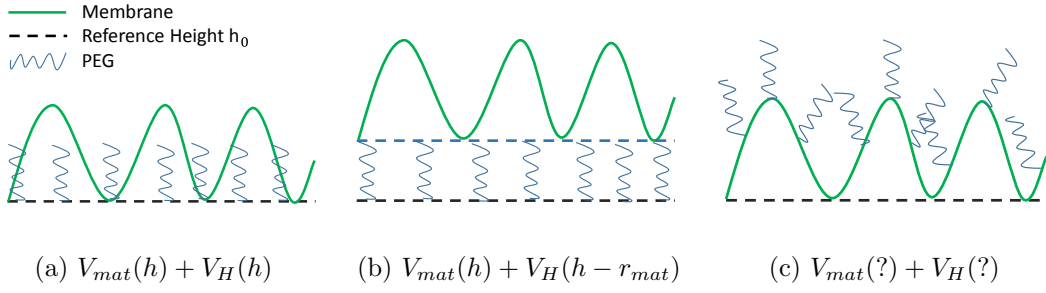


Figure 16: Different ways of describing the additivity of Helfrich and polymer steric repulsion.

5 Outlook

We have seen that a fluctuating membrane doesn't necessarily sit in the minimum of an external potential due to its fluctuations. This issue is addressed by the Helfrich repulsion, which works perfectly fine for a membrane that is pressured against a wall or captured between two walls. As soon as we introduce a more complicated external potential and PEG molecules on the membrane, and this is a standard procedure in experiments, the additivity of Helfrich repulsion and external potential break down. Figure 16 (a) and (b) show the center of the problem. Depending on where we set $h - r_{mat}$ for the Helfrich potential, we can achieve results closer to the simulated results, but we can't reproduce the reality where the PEG is part of the fluctuations. PEG as part of the membrane is displayed in Figure 16 (c) and shows that PEG is more influential on the peaks of the membrane than in the valleys. Another argument that also illustrates the issue with additivity is whether V_{mat} or V_H should be altered,

$$V_{mat}(h - h_H) \neq V_H(h - h_{mat}),$$

either shifting V_{PEG} by the characterizing height for the Helfrich repulsion or shifting V_H by the characterizing height for the polymer steric repulsion. This issue has to be addressed by more complicated simulations, which include actual PEG molecules on the surface of the fluctuating membrane and can not be dealt with by using additivity and

approximated potentials. Another way to address the problem is to bring experimental and theoretical approaches closer together. A reduction of complexity in the experimental setup would be easier to implement in a theoretical framework and therefore the comparison of results would be easier.

Despite showing that this phenomenon is still unresolved from a theoretical standpoint, we were able to reproduce experimental results with our Monte Carlo simulations. As the input for the Monte Carlo simulations is known, we have found the basic principles which cause the phenomenon in the experiments: The polymer steric repulsion caused by the PEG on the membrane keeps the membrane far enough from the surface to avoid most of the divergence of the van der Waals attraction. This effect generates a potential in which the membrane fluctuations are sufficient to avoid resting in the minimum of the external potential. By finding the fundamental principles that cause this phenomenon we made the first big step in the direction of developing a comprehensive theory to describe membrane interaction principles.

References

- [1] Barone, V. & Heisenberg, C.-P. Cell adhesion in embryo morphogenesis. *Current opinion in cell biology* **24**, 148–53 (2012).
- [2] Bendas, G. & Borsig, L. Cancer cell adhesion and metastasis: selectins, integrins, and the inhibitory potential of heparins. *International journal of cell biology* **2012**, 676731 (2012).
- [3] Lafrenie, R., Buchanan, M. & Orr, F. Adhesion molecules and their role in cancer metastasis. *Cell biophysics* **23**, 3–89 (1993).
- [4] Zhang, Y. Stealth Liposomes: the silent nanobombers. *Preclinical Formulation - Trends in Bio/Pharmaceutical Industry* **4**, 19–24 (2008).
- [5] Eukaryotic Cell. URL [https://upload.wikimedia.org/wikipedia/commons/3/3e/Eukaryotic_Cell_\(animal\).jpg](https://upload.wikimedia.org/wikipedia/commons/3/3e/Eukaryotic_Cell_(animal).jpg).
- [6] Lodish, H. *et al. Molecular Cell Biology* (W. H. Freeman, 2000).
- [7] Gönnerwein, S. *Generic and Specific Cell Adhesion: Micro-Interferometry* (Universitätsbibliothek der TU München, 2003).
- [8] Alberts, B. *et al. Molecular Biology of the Cell* (Garland Science, 2002).
- [9] Lipowsky, R. The conformation of membranes. *Nature* **349**, 475–481 (1991).
- [10] Tanaka, M. & Sackmann, E. Polymer-supported membranes as models of the cell surface. *Nature* **437**, 656–663 (2005).
- [11] Fenz, S. & Sengupta, K. Giant vesicles as cell models. *Integrative biology : quantitative biosciences from nano to macro* **4**, 982–95 (2012).
- [12] Brown, F. Elastic Modeling of Biomembranes and Lipid Bilayers. *Annual Review of Physical Chemistry* **59**, 685–712 (2008).

- [13] Prost, J., Manneville, J.-B. & Bruinsma, R. Fluctuation-magnification of non-equilibrium membranes near a wall. *The European Physical Journal B* **1**, 465–480 (1998).
- [14] Sabra, M. & Mouritsen, O. Steady-state compartmentalization of lipid membranes by active proteins. *Biophysical Journal* **74**, 745–752 (1998).
- [15] Canham, P. The minimum energy of bending as a possible explanation of the biconcave shape of the human red blood cell. *Journal of Theoretical Biology* **26**, 61–81 (1970).
- [16] Helfrich, W. Elastic properties of lipid bilayers: theory and possible experiments. *Zeitschrift fur Naturforschung. Teil C: Biochemie, Biophysik, Biologie, Virologie* **28**, 693–703 (1973).
- [17] Seifert, U. Configurations of fluid membranes and vesicles. *Advances in Physics* **46**, 13–137 (1997).
- [18] Bruinsma, R., Behrisch, A. & Sackmann, E. Adhesive switching of membranes: experiment and theory. *Physical review. E, Statistical physics, plasmas, fluids, and related interdisciplinary topics* **61**, 4253–4267 (2000).
- [19] Fenz, S., Merkel, R. & Sengupta, K. Diffusion and intermembrane distance: Case study of avidin and E-cadherin mediated adhesion. *Langmuir* **25**, 1074–1085 (2009).
- [20] Limozin, L. & Sengupta, K. Quantitative reflection interference contrast microscopy (RICM) in soft matter and cell adhesion. *Chemphyschem: a European journal of chemical physics and physical chemistry* **10**, 2752–68 (2009).
- [21] Curtis, A. The Mechanism of Adhesion of Cells to Glass: A Study by Interference Reflection Microscopy. *The Journal of Cell Biology* **20**, 199–215 (1964).

- [22] Verschueren, H. Interference reflection microscopy in cell biology: methodology and applications. *Journal of cell science* **75**, 279–301 (1985).
- [23] Geiger, B., Avnur, Z., Kreis, T. & Schlessinger, J. The dynamics of cytoskeletal organization in areas of cell contact. *Cell and muscle motility* **5**, 195–234 (1984).
- [24] Bereiter-Hahn, J. Quantitative reflection contrast microscopy of living cells. *The Journal of Cell Biology* **82**, 767–779 (1979).
- [25] Monzel, C., Fenz, S., Giesen, M., Merkel, R. & Sengupta, K. Mapping fluctuations in biomembranes adhered to micropatterns. *Soft Matter* **8**, 6128 (2012).
- [26] Bruinsma, R., Goulian, M. & Pincus, P. Self-assembly of membrane junctions. *Biophysical journal* **67**, 746–750 (1994).
- [27] Weikl, T. R. Dynamic phase separation of fluid membranes with rigid inclusions. *Phys. Rev. E* **66**, 61915 (2002).
- [28] Bihr, T. *et al.* Association rates of membrane-coupled cell adhesion molecules. *Biophysical journal* **107**, L33–6 (2014).
- [29] Schmidt, D., Bihr, T., Seifert, U. & Smith, A.-S. Coexistence of dilute and densely packed domains of ligand-receptor bonds in membrane adhesion. *EPL (Europhysics Letters)* **99**, 38003 (2012).
- [30] Andelman, D. Electrostatic Properties of Membranes: The Poisson – Boltzmann Theory. *Handbook of Biological Physics* **1**, 603–641 (1995).
- [31] Schneck, E. & Netz, R. From simple surface models to lipid membranes: Universal aspects of the hydration interaction from solvent-explicit simulations. *Current Opinion in Colloid and Interface Science* **16**, 607–611 (2011).
- [32] Van Oss, C., Chaudhury, M. & Good, R. Interfacial Lifshitz-van der Waals and polar interactions in macroscopic systems. *Chemical Reviews* **88**, 927–941 (1988).

- [33] Hamaker, H. The London-van der Waals attraction between spherical particles. *Physica* **4**, 1058–1072 (1937).
- [34] Schmidt, D. *et al.* Signature of a Nonharmonic Potential as Revealed from a Consistent Shape and Fluctuation Analysis of an Adherent Membrane. *Physical Review X* **4**, 021023 (2014).
- [35] Auth, T., Safran, S. A. & Gov, N. Fluctuations of coupled fluid and solid membranes with application to red blood cells. *Physical review. E, Statistical, nonlinear, and soft matter physics* **76**, 051910 (2007).
- [36] Pierres, A., Benoliel, A.-M., Touchard, D. & Bongrand, P. How cells tiptoe on adhesive surfaces before sticking. *Biophysical journal* **94**, 4114–22 (2008).
- [37] Safran, S., Gov, N., Nicolas, A., Schwarz, U. & Tlusty, T. Physics of cell elasticity, shape and adhesion. *Physica A: Statistical Mechanics and its Applications* **352**, 171–201 (2005).
- [38] Lu, B.-S. & Podgornik, R. Effective interactions between fluid membranes. *Physical Review E* **92**, 022112 (2015).
- [39] Helfrich, W. Steric interaction of fluid membranes in multilayer systems. *Zeitschrift für Naturforschung A* **5** (1978).
- [40] Janke, W. & Kleinert, H. Fluctuation pressure of membrane between walls. *Physics Letters A* **117**, 353–357 (1986).
- [41] Bachmann, M., Kleinert, H. & Pelster, A. Variational perturbation theory for density matrices. *Physical Review A* **60**, 3429–3443 (1999).
- [42] Bachmann, M., Kleinert, H. & Pelster, a. Fluctuation pressure of a stack of membranes. *Physical Review E* **63**, 051709 (2001).

- [43] Marx, S., Schilling, J., Sackmann, E. & Bruinsma, R. Helfrich repulsion and dynamical phase separation of multicomponent lipid bilayers. *Physical review letters* **88**, 138102 (2002).
- [44] Parsegian, V. *Van der Waals Forces - A Handbook for Biologists, Chemists, Engineers, and Physicists* (Cambridge University Press, Cambridge, 2006).
- [45] Smith, E. R., Mitchell, D. & Ninham, B. Deviations of the van der Waals Energy for Two Interacting Spheres from the Predictions of Hamaker Theory. *Journal of Colloid and Interface Science* **45** (1973).
- [46] Israelachvili, J. *Intermolecular and Surface Forces* (Elsevier, 2011).
- [47] Dagastine, R., Prieve, D. & White, L. The Dielectric Function for Water and Its Application to van der Waals Forces. *Journal of colloid and interface science* **231**, 351–358 (2000).
- [48] Parsegian, V. & Ninham, B. Van der Waals forces in many-layered structures: Generalizations of the lifshitz result for two semi-infinite media. *Journal of Theoretical Biology* **38**, 101–109 (1973).
- [49] Abramowitz, M. & Irene, S. *Handbook of mathematical functions* (National Bureau of Standards Applied Mathematics Series, 1965).
- [50] Attard, P., Mitchell, D. & Ninham, B. The attractive forces between polar lipid bilayers. *Biophysical journal* **53**, 457–460 (1988).
- [51] Masuda, T., Matsuki, Y. & Shimoda, T. Spectral parameters and Hamaker constants of silicon hydride compounds and organic solvents. *Journal of colloid and interface science* **340**, 298–305 (2009).
- [52] Parsegian, V. & Weiss, G. Spectroscopic parameters for computation of van der waals forces. *Journal of Colloid and Interface Science* **81**, 285–289 (1981).

- [53] Roth, C. & Lenhoff, A. Improved Parametric Representation of Water Dielectric Data for Lifshitz Theory Calculations. *Journal of Colloid and Interface Science* **179**, 637–639 (1996).
- [54] Eden, J., Gascoyne, P. & Pethig, R. Dielectric and electrical properties of hydrated bovine serum albumin. *Journal of the Chemical Society* 426–434 (1980).
- [55] Mali, C., Chavan, S., Kanse, K., Kumbharkhane, A. & Mehrotra, S. Dielectric relaxation of poly ethylene glycol-water mixtures using time domain technique. *Indian Journal of Pure & Applied Physics* **45**, 476–481 (2007).
- [56] Looyenga, H. Dielectric constants of heterogeneous mixtures. *Physica* **31**, 401–406 (1965).
- [57] Aspnes, D. E. Optical properties of thin films. *Thin Solid Films* **89**, 249–262 (1982).
- [58] Robertson, W. M., Arjavalingham, G. & Shinde, S. L. Microwave dielectric measurements of zirconia-alumina ceramic composites: A test of the Clausius-Mossotti mixture equations. *Journal of Applied Physics* **70**, 7648–7650 (1991).
- [59] Avanti Polar Lipids, Inc. PEG 2000 Avanti. URL https://www.avantilipids.com/index.php?option=com_content&view=article&id=1088&Itemid=448&catnumber=880120.
- [60] Hannay, J. The Clausius-Mossotti equation: an alternative derivation. *European Journal of Physics* **141** (1983).
- [61] Parsons, D. & Ninham, B. Importance of accurate dynamic polarizabilities for the ionic dispersion interactions of alkali halides. *Langmuir : the ACS journal of surfaces and colloids* **26**, 1816–23 (2010).
- [62] H.-J. Werner *et al.* Molpro, version 2008.1, a package of ab initio programs. URL <http://www.molpro.net/>.

- [63] TURBOMOLE V6.4 2012, a development of University of Karlsruhe and Forschungszentrum Karlsruhe GmbH, 1989–2007, TURBOMOLE GmbH, since 2007. URL <http://www.turbomole.com/>.
- [64] Lipowsky, R. *Generic Interactions of Flexible Membranes*, vol. 1 (Elsevier, 1995).
- [65] Rädler, J., Feder, T., Strey, H. & Sackmann, E. Fluctuation analysis of tension-controlled undulation forces between giant vesicles and solid substrates. *Physical Review E* **51**, 4526–4536 (1995).
- [66] Matlab R-Square Error, Goodness-of-Fit Statistics. URL http://de.mathworks.com/help/curvefit/evaluating-goodness-of-fit.html#bq_5kwr-3.
- [67] Gompper, G. & Kroll, D. Steric Interactions in Multimembrane Systems: A Monte Carlo Study. *EPL (Europhysics Letters)* **9**, 59–64 (1989).
- [68] Gouliaev, N. & Nagle, J. Simulations of a single membrane between two walls using a Monte Carlo method. *Physical Review E* **58**, 881–888 (1998).
- [69] Auth, T. & Gompper, G. Fluctuation pressure of biomembranes in planar confinement. *Physical Review E* **88**, 010701 (2013).
- [70] Shiba, H., Noguchi, H. & Fournier, J.-B. Monte Carlo study of the frame, fluctuation and internal tensions of fluctuating membranes with fixed area (2015). arXiv:1507.08722[cond-mat.soft].
- [71] GSL - GNU Scientific Library, A numerical library for C and C++ under the GNU General Public License. URL <http://www.gnu.org/software/gsl/>.
- [72] Mecke, K. & Charitat, T. Fluctuating Lipid Bilayer in an Arbitrary Potential. *Langmuir* **19**, 2080–2087 (2003).
- [73] Weikl, T. & Lipowsky, R. *Membrane adhesion and domain formation* (Elsevier, 2006).

- [74] Parsons, D., Walsh, R. & Craig, V. Surface forces: surface roughness in theory and experiment. *The Journal of chemical physics* **140**, 164701 (2014).
- [75] Sackmann, E. Supported membranes: scientific and practical applications. *Science (New York, N.Y.)* **271**, 43–48 (1996).
- [76] Garbuzenko, O., Barenholz, Y. & Prie, A. Effect of grafted PEG on liposome size and on compressibility and packing of lipid bilayer. *Chemistry and Physics of Lipids* **135**, 117–129 (2005).
- [77] Hansen, P., Cohen, J., Podgornik, R. & Parsegian, V. Osmotic properties of poly(ethylene glycols): quantitative features of brush and bulk scaling laws. *Biophysical journal* **84**, 350–355 (2003).
- [78] Kenworthy, K., Hristova, K., Needham, D. & McIntosh, T. Range and magnitude of the steric pressure between bilayers containing phospholipids with covalently attached poly(ethylene glycol). *Biophysical journal* **68**, 1921–1936 (1995).
- [79] Evans, E. & Rawicz, W. Entropy-driven tension and bending elasticity in condensed-fluid membranes. *Physical review letters* **64**, 2094–2097 (1990).
- [80] Ly, H. & Longo, M. The influence of short-chain alcohols on interfacial tension, mechanical properties, area/molecule, and permeability of fluid lipid bilayers. *Biophysical journal* **87**, 1013–1033 (2004).

Eidesstattliche Erklärung

Hiermit erkläre ich, dass ich die vorliegende Arbeit selbst verfasst und keine anderen als die angegebenen Quellen und Hilfsmittel verwendet habe.

Ort, Datum

Unterschrift